This is the accepted manuscript made available via CHORUS. The article has been published as:

Robust block magnetism in the spin ladder compound BaFe_{2}Se_{3} under hydrostatic pressure

Shan Wu, Junjie Yin, Thomas Smart, Arani Acharya, Craig L. Bull, Nicholas P. Funnell, Thomas R. Forrest, Gediminas Simutis, Rustem Khasanov, Sylvia K. Lewin, Meng Wang, Benjamin A. Frandsen, Raymond Jeanloz, and Robert J. Birgeneau

Phys. Rev. B **100**, 214511 — Published 20 December 2019

DOI: 10.1103/PhysRevB.100.214511

Robust block magnetism in the spin ladder compound $BaFe_2Se_3$ under hydrostatic pressure

Shan Wu,[1,*] Junjie Yin,[2] Thomas Smart,[3] Arani Acharya,[1] Craig L Bull,[4] Nicholas P Funnell,[4] Thomas R Forrest,[5] Gediminas Simutis,[6] Rustem Khasanov,[6] Sylvia K. Lewin,[1] Meng Wang,[2] Benjamin A. Frandsen,[7] Raymond Jeanloz,[3] and Robert J. Birgeneau[1]

[1]*Department of Physics, University of California, Berkeley, California, 94720, USA*
[2]*School of Physics, Sun Yat-Sen University, Guangzhou 510275, China*
[3]*Department of Earth and Planetary Science, University of California, Berkeley, California, 94720, USA*
[4]*ISIS Neutron and Muon Facility, Rutherford Appleton Laboratory, Chilton, Oxon, UK.*
[5]*Diamond Light Source, Chilton, Oxon, UK*
[6]*Laboratory for Muon Spin Spectroscopy, Paul Scherrer Institute, Villigen, PSI, Switzerland*
[7]*Department of Physics, Brigham Young University, Provo, Utah 84602, USA*

(Dated: November 19, 2019)

The majority of the iron-based superconductors (FeSCs) exhibit a two-dimensional square lattice structure. Recent reports of pressure-induced superconductivity in the spin-ladder system, $BaFe_2X_3$ (X =S,Se), introduce a quasi-one-dimensional prototype and an insulating parent compound to the FeSCs. Here we report X-ray, neutron diffraction and muon spin relaxation experiments on $BaFe_2Se_3$ under hydrostatic pressure to investigate its magnetic and structural properties across the pressure-temperature phase diagram. A structural phase transition was found at a pressure of 3.7(3) GPa. Neutron diffraction measurements at 6.8(3) GPa and 120 K show that the block magnetism persists even at these high pressures. A steady increase and then fast drop of the magnetic transition temperature T_N and greatly reduced moment above the pressure P_s indicate potentially rich and competing phases close to the superconducting phase in this ladder system.

I. INTRODUCTION

In correlated electron materials, applied pressure or chemical substitution can alter the electronic structure and, concomitantly, the electron correlations, leading to a wide variety of electronic phases and phase transitions. These include metal-insulator transitions, charge density wave order, antiferromagnetism, and superconductivity (SC)[1–7]. In iron-based superconductors, optimal superconductivity typically appears when the magnetic order is suppressed by the doping of carriers. The recent discovery of pressure-induced SC around a critical pressure (P_c) of 10 GPa with the superconducting temperature T_c up to 24 K in $BaFe_2X_3$(X = S,Se)[8–10] provides a new venue for documenting the connection between magnetism and superconductivity without introducing any disorder by chemical doping. Importantly, these materials display a quasi-one-dimensional (1D) iron ladder structure[11,12] rather than the more usual square planar structure, and the parent compounds are insulators rather than poor metals. The reduced dimensionality and the metal-insulator transition preceding the superconducting phase resemble the characteristics of the cuprate system $Sr_{14-x}Ca_xCu_{24}O_{41}$[3,13]. These ladder materials can thus provide important insights into the similarities and differences for both copper and iron-based superconductors.

Extensive experimental and theoretical work has been carried out on the parent compounds $BaFe_2X_3$(X = S,Se) at ambient pressure[14–22]. In $BaFe_2S_3$, stripe-type antiferromagnetic (AFM) order (Fig. 1 (a)) has been found below the Néel temperature (T_N) of 119 K[8,9]. In contrast, $BaFe_2Se_3$ shows an exotic block-type magnetic order below 255 K[11,12]. The origin of this magnetic structure was ascribed theoretically to an orbital-selective Mott phase (OSMP) from multi-orbital Hubbard models for a 1D system[21,23,24]; the spin dynamics probed by inelastic neutron scattering[14] are consistent with this picture. Theoretical proposals of magnetic ferri-electricity[15] and the macroscopic polarization due to a block-type lattice distortion[20] may suggest the importance of electronic contributions to the block state embedded within the OSMP phase.

Recent studies of the pressure-temperature (P-T) phase diagram by local magnetic probes have focused primarily on $BaFe_2S_3$, the first Fe-based spin-ladder system for which pressure-induced superconductivity was reported[25–27]. In $BaFe_2Se_3$, limited pressure-dependent experimental work has been carried out beyond transport measurements. The lack of information on the magnetic properties across the P-T phase diagram is particularly notable. This is a result of the experimental challenges of performing neutron diffraction experiments at simultaneous conditions of high pressure (beyond 2 GPa) and cryogenic temperatures, leaving a crucial gap in experimental characterization of the iron-based spin ladder systems. In addition, the sensitivity of the magnetism to the local structure and stoichiometry in different samples may produce varied magnetic behaviors[26,28]. Thus, studies on the same sample are essential to establish a unified P-T phase diagram.

In this paper, we present a comprehensive characterization of the magneto-structural properties of $BaFe_2Se_3$ across a large region of the P-T phase diagram

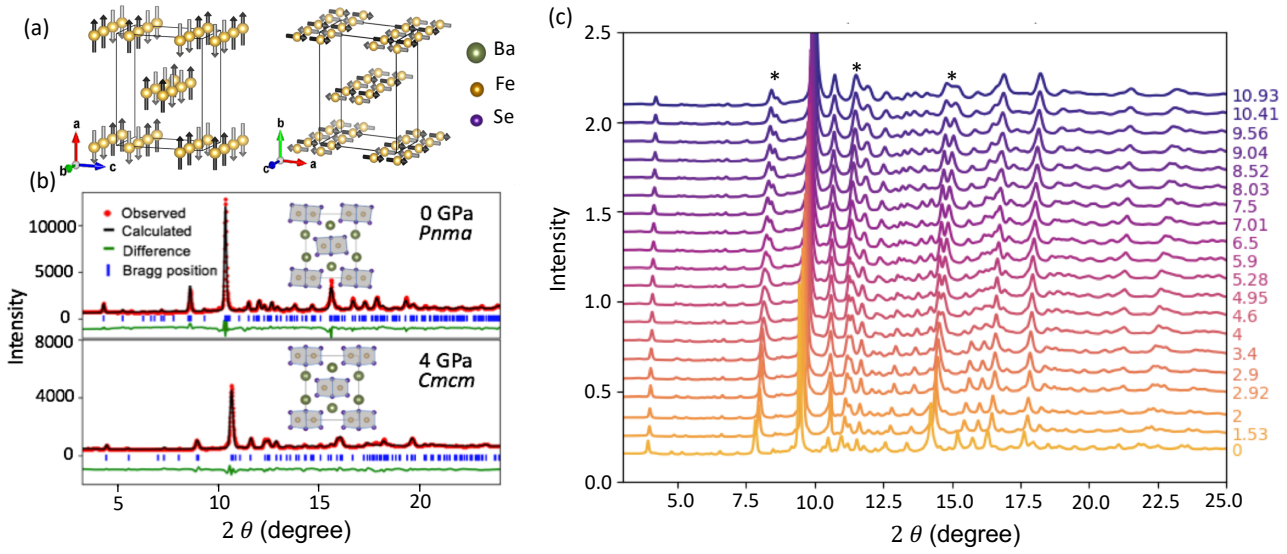

FIG. 1: (a) Sketch of the block-type (left) and stripe-type (right) magnetic orders. (b) Room temperature X-ray diffraction patterns for $BaFe_2Se_3$ at $P = 0$ and 4 GPa, fitted with $Pnma$ and $Cmcm$ models, respectively. Insets show corresponding structures viewed along the ladder direction. (c) Pressure-dependent X-ray powder diffraction patterns from $P = 10.93$ GPa to ambient pressure (decompression data). The values shown on the right of the plot are in the unit of GPa. Asterisks indicate the peaks that show evidence of a crystal-structural transformation.

using three complementary experimental probes at various pressure and temperature conditions: neutron powder diffraction (NPD) with pressures up to 6.8 GPa and temperatures down to 120 K, muon spin relaxation (μSR) measurements up to 2.43 GPa and down to 10 K, and X-ray powder diffraction (XRD) measurements up to 12 GPa at ambient temperature. Our measurements identify a structural transition from the $Pnma$ to $Cmcm$ space group at P_s =3.7(3) GPa. We observe a gradual enhancement of T_N with pressure up to P_s, similar to $BaFe_2S_3$[26], followed by a considerable reduction of T_N above P_s. Intriguingly, the block-type magnetism in $BaFe_2Se_3$ remains stable up to the highest pressure measured by NPD (6.8 GPa), despite the fact that the crystallographic structure above P_s is identical to that of $BaFe_2S_3$ with stripe-type magnetism. Comparing the similarities and differences between these two ladder compounds yields important insights into the origin of the unusual block-type magnetism, the role of electronic correlations and orbital selectivity, and potentially the mechanism of superconductivity in these systems, greatly enriching the discussion of magnetism and superconductivity in iron-based materials.

II. METHODS

A powder sample of $BaFe_2Se_3$ was synthesized by a self-flux solid state reaction[11]. Powder diffraction data at ambient pressure were collected on HB3A, HFIR. Neutron diffraction measurements under pressure employed the Pearl diffractometer with a Paris-Edinburgh (PE) press at the ISIS Pulsed neutron and Muon source, UK[29]. A mixture of $BaFe_2Se_3$ and lead powder was pressed in a single-toroidal zirconia-toughened alumina anvil with Ti-Zr gaskets for pressures below 6 GPa and a sintered diamond anvil cell (DAC) above 6 GPa. Hydrostatic pressure was provided with a pressure-transmitting fluid of pre-deuterated methanol/ethanol mixture in a 4:1 volume ratio. The base temperature could reach 120 K with an uncertainty of 2-3 K. The pressure was calibrated with the lattice constant of the lead with an uncertainty in the measured pressure of 0.3 GPa. The intensities have been normalized to the incident beam monitor for one hour and corrected for the detector efficiency.

Muon spin relaxation (μSR) spectroscopy was performed on samples under pressure using the general purpose decay-channel (GPD) instrument at the Paul Scherrer Institute, Switzerland[30]. The body of the pressure cell used a MP35N(Ni-Co-Cr-Mo) alloy. Daphne oil was used as pressure-transmitting fluid. The pressure was calibrated with a superconducting indium plate immersed in the oil with an uncertainty in the measured pressure less than 0.1 GPa.

Room temperature pressure-dependent X-ray diffraction was performed at the beam line 12.2.2, Advanced Light Source, Lawrence Berkeley National Laboratory. We loaded the mixture of the sample and ruby powder into a Merrill-Basset DAC with a steel gasket and 4:1 methanol/ethanol pressure-transmitting fluid. The pressure was calibrated by the ruby fluorescence R1-line with accuracy of 0.1 GPa.

III. RESULTS

A. X-ray diffraction

The XRD pattern at ambient conditions (Fig. 1(b)) is well described by the expected *Pnma* structure, as verified by Rietveld refinements using the FULLPROF Suite[31] with $\chi^2 = 6.4$, giving a better fit than *Cmcm* (χ^2 = 8.6). At $P = 4$ GPa, the *Cmcm* structure provides a significantly better fit ($\chi^2 = 2.8$) than does *Pnma* (χ^2 = 6.6). The main difference between the two structures is that the ladder plane is tilted with respect to the crystallographic a axis in the *Pnma* structure (inset of Fig. 1 (b)). NPD data, to be described subsequently, confirm the structural transition. The critical pressure marking the transition from *Pnma* to *Cmcm* is estimated to be 3.7(3) GPa, based on inspection of the diffraction patterns at several decompressed pressures (Fig. 1 (c)). The higher crystallographic symmetry of the *Cmcm* phase leads to a reduced number of Bragg peak positions. For example, at the position of $2\theta \sim 7.6°$ the peak is indexed as the superposition of Bragg peak (211), (301) and (202) in the *Pnma* phase, while the (211) peak is forbidden in the *Cmcm* phase. The corresponding pressure dependence of the refined lattice parameters (Fig. 5 (c-d)) displays a change of slope marked by the results of linear fits. This structural transition agrees with previous results[32].

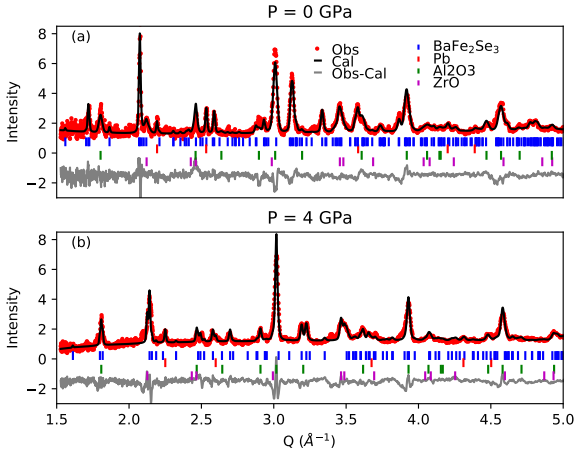

FIG. 2: Room temperature neutron powder diffraction data (red dots) at $P = 0$ and 4 GPa collected in the transverse mode (Pearl diffractometer, ISIS) and their corresponding Rietveld refinements (black lines). Vertical bars denote the contributions from the $BaFe_2Se_3$, Pb for the calibration and materials of the pressure cell.

B. Neutron diffraction

Neutron diffraction measurements were performed under ambient pressure and pressures of 2.1, 4 ,5.5 and 6.8 GPa in two detector modes: longitudinal and transverse. The transverse mode involves nine detectors located perpendicular to the beam path, and covers the range $1.5Å^{-1} < Q < 5Å^{-1}$. This mode is used for the structural refinement; representative patterns are shown in Fig. 2 for pressures of $P = 0$ and 4 GPa. The data are fitted with the space group *Pnma* (Fig. 2 (a)) and *Cmcm* (Fig. 2 (b)) respectively, consistent with XRD refinements under pressure in Fig. 1 (b), and again confirming the structural transition at $P_s = 3.7(3)$ GPa. The fitting patterns include the phases from the lead powder used for the pressure calibration and the pressure cell made from mixture of pollycrystallines Al_2O_3 and ZrO.

Alternatively, the longitudinal mode, with three detectors aligned along the beam path, allows access to low wave vector transfer Q down to about 0.6 $Å^{-1}$. The significantly reduced intensity in the longitudinal mode necessitates counting for several hours to achieve adequate statistics for each diffraction pattern. In Fig. 3, we present NPD patterns at various pressures and temperatures collected in this configuration. The significantly reduced intensity in this mode necessitates counting for several hours to achieve adequate statistics for each diffraction pattern. The intensities have been normalized to the incident beam monitor for one hour and corrected for the detector efficiency. At ambient pressure, the diffraction patterns collected at $T = 225$ K and below show an additional Bragg reflection at $Q \approx 0.74$ $Å^{-1}$, which can be indexed as $Q_{m1} = (\frac{1}{2}\frac{1}{2}\frac{1}{2})$. The calculated pattern (Fig. 3 (f)I) is consistent with an Fe_4 block-type spin structure[11,12,33]. Rietveld refinement of the NPD data collected on HB3A at 1.5 K confirms it and yields a refined ordered moment of 2.9(3) μ_B/Fe and transition temperature $T_N = 250(5)$ K.

With increasing pressure, this magnetic peak (broad hump for the highest two pressures) shown in Fig. 3 (a-e) persists, indicating that the Fe_4 block magnetic state persists to the highest attainable pressure of 6.8 GPa. At $P = 0$, 2.1 and 4 GPa, this peak displays a full width at half maximum (FWHM) value similar to that of the nearby nuclear Bragg peak (the horizontal bar in Fig. 3 (a-c)). However, at $P = 5.5$ and 6.8 GPa, the width of this magnetic peak is almost twice as wide as the instrumental Q-resolution of $0.025(2)Å^{-1}$ (Fig. 3 (d-e)). Such broadening implies a crossover to short-range, block-type magnetic correlations, suggesting that any transition to true long-range magnetic order occurs below 120 K for 5.5 and 6.8 GPa.

At $P = 4$ GPa ($> P_s$), the integrated intensity around Q_{m1} is significantly reduced (33%) compared to that at lower pressures, indicating a significant suppression of the ordered magnetic moment after the structural transition. Due to limited momentum access to magnetic peaks with

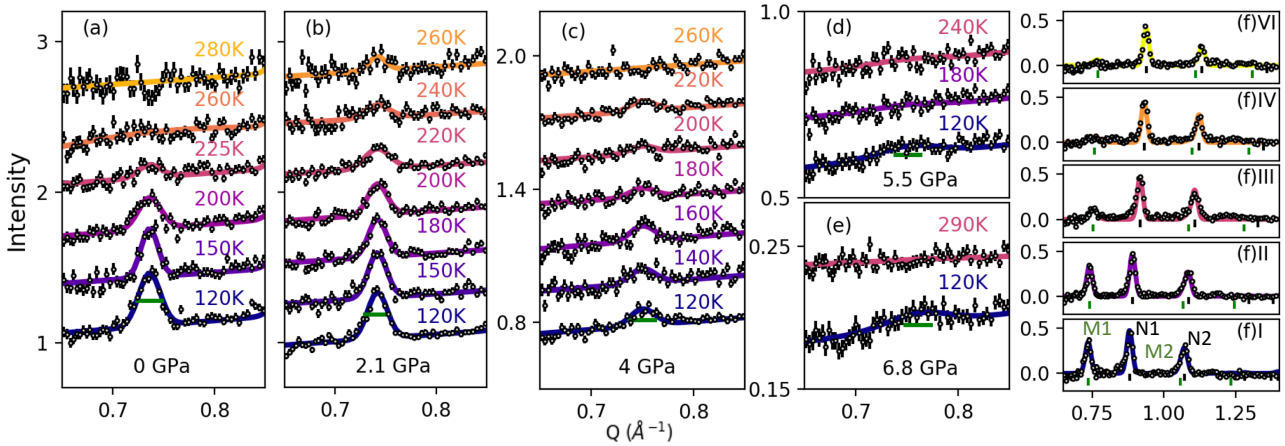

FIG. 3: Temperature dependence of neutron powder diffraction (NPD) data for $BaFe_2Se_3$ at pressures of 0 (a), 2.1 (b), 4 (c) 5.5 (d), and 6.8 GPa (e) collected at Pearl, ISIS[29]. The additional peak at wave vector $Q \approx 0.75$ Å^{-1} that appears at low temperature can be indexed as $Q_{m1} = (0.5,0.5,0.5)$, consistent with the Fe_4 block spin structure. The data are normalized to 1 hour counting time and shifted a constant value vertically at each pressure for clarity. The solid curves are the results of fits using a single Gaussian peak. The horizontal bar represents the instrument resolution of 0.024 Å^{-1} determined from a nearby nuclear Bragg peak. (f) Zoomed-out view of the NPD patterns at $T = 120$ K for all pressures (0 to 6.8 GPa from the bottom to top). The colored curves are calculated patterns including both nuclear and magnetic phases. The peak positions with sufficient calculated/observed intensity are marked by vertical black (N1:(101), N2:(200)) and green lines (M1:$(\frac{1}{2}\frac{1}{2}\frac{1}{2})$, M2:$(\frac{3}{2}\frac{1}{2}\frac{1}{2})$).

clean background in the measured mode, a conventional Rietveld analysis is difficult to perform on the NPD data. Assuming the block-type magnetic structure but varying the spin orientation with respect to the ladder axis, the fits to the data (Fig. 3 (f)III) for the first two magnetic peaks (Q_{m1},$Q_{m2} = (\frac{3}{2}\frac{1}{2}\frac{1}{2})$) display slightly better results with spins pointing perpendicular to the ladder direction (a or b axis) rather than along the ladder direction (c axis). Importantly, above P_s, there is no clear observation of any magnetic signal associated with the stripe-type order found in $BaFe_2S_3$. Bragg peaks resulting from this magnetic structure would be indexed by the fundamental wave vector $k = (\frac{1}{2}, \frac{1}{2}, 0)$ and would contribute significant intensity at $Q = 0.939$Å^{-1} for spins oriented along the c axis and 1.27 Å^{-1} for spins along the a or b axes. Given statistics of the NPD data, we place an upper limit of 0.3 μ_B for any stripe-type moment. This contrasts with $BaFe_2S_3$, where stripe-type order is observed throughout the $Cmcm$ phase, and demonstrates that the structural symmetry is not solely responsible for the block-type state in $BaFe_2Se_3$.

C. Muon spin relaxation

As for the pressure-dependence of T_N, the Q_{m1} peak at $T = 260$ K is observed at 2.1 GPa but not 0 GPa (Fig. 3(a-b)), indicating an increase in T_N with increasing pressure in the $Pnma$ phase. To verify this finding, we now turn to pressure-dependent μSR measurements, which have finer control on the pressure and temperature steps. Importantly, we utilized the same powder sample as was used for the NPD experiments. In Fig. 4 (a-f), we display temperature-dependent μSR spectra from ambient pressure up to 2.43 GPa collected in a zero field (ZF) configuration. The initial drop of the total asymmetry at low temperatures compared to that at room temperature originates from the long-range magnetic order; from this drop, we can obtain the magnetically ordered volume fraction under various pressures. The lack of clear oscillations of the asymmetry, in contrast to muon results for $BaFe_2S_3$[26], could be attributed to the block-type ordered state that yields a distribution of different muon stopping sites and/or a larger field magnitude at the muon stopping sites. We modelled the ZF μSR spectra with an exponentially relaxing component and a Kubo-Toyabe component, corresponding to muons stopping in the sample and the sample holder, respectively[30].

We can also determine the magnetic volume fraction from μSR measurement by applying a weak transverse field (wTF) of 50 Gauss. Representative wTF spectra for several temperatures under one pressurized condition are shown in Fig. 4 (g). For $T > T_N$, the cosine oscillations are the response from the paramagnetic state of the sample and the pressure cell in applied wTF. For $T \leq T_N$, the reduced oscillation amplitude is associated with the 1/3 of magnetically ordered volume fraction f. The asymmetry, thus, can be described as: $P(t) = A[\frac{1}{3}fe^{-\lambda_1 t} + (1-f)cos(\gamma_\mu Bt)e^{-\lambda_2 t}] + P(t)_{NP}$. Here A is the total asymmetry; B is the applied external weak transverse field; λ_1 and λ_2 are the longitudinal relaxation rate due to the internal field fluctuating in time and paramagnetic spin fluctuations respectively. $P(t)_{NP}$ is the portion from the pressure cell which follows the revised Gaussian depolarization function[30]. The static and dynamic relaxation rates from the pressure cell are interpolated according to the literature[30].

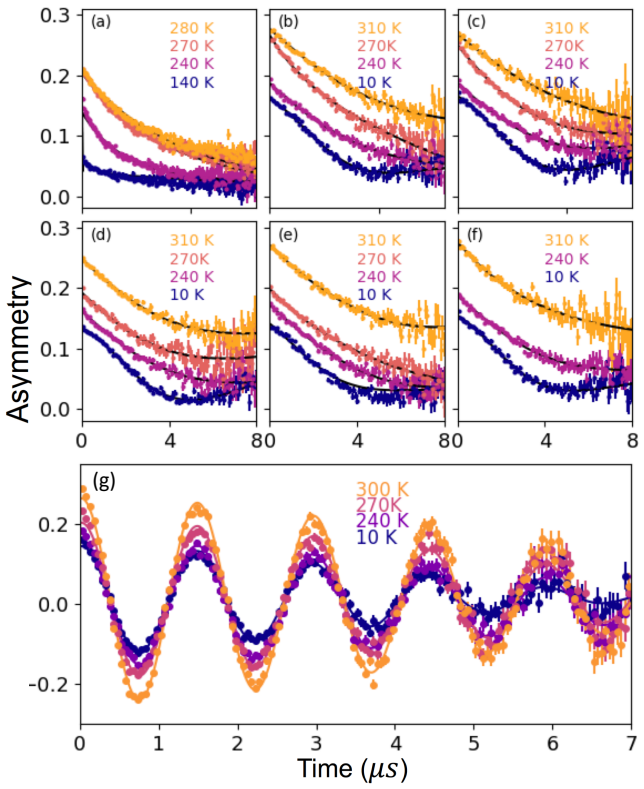

FIG. 4: Representative temperature-dependent μSR spectra for $BaFe_2Se_3$ at ambient pressure (a) and measured pressures of 0.19 (b), 0.76 (c), 1.67 (d), 2.03 (e), and 2.43 GPa (f) in zero field (ZF). Data from ambient pressure and hydrostatic pressure conditions were collected at TRIUMF and PSI, respectively. The color dots represent data collected at different temperatures and the black lines represent results of fits to the data. (g) Representative weak transverse field (50 Tesla) spectra and corresponding fittings at 1.67 GPa for several temperatures.

All fits for ZF and wTF spectra were performed using the MUSRFIT package[34]. From these refinements, we extracted the magnetic volume fraction as a function of temperature for pressures up to 2.43 GPa. The results are displayed in Fig. 5 (b). A bulk magnetic transition is manifest as a large increase in the magnetic volume fraction as the temperature is lowered. With increasing pressure from 0 to 2.43 GPa, we observe the magnetic transition gradually moving to higher temperature, confirming an increase in T_N with pressure in this range. We quantify T_N at each pressure by defining it as the midpoint of the temperature region where the magnetic volume fraction is changing (black star in Fig. 5 (b)). The error bars are fixed at 20% of the width of the temperature region where the magnetic fraction changes. We note that the observed magnetic fraction remains close to 1 at low temperature for all pressures, implying a fully ordered state below T_N.

IV. DISCUSSIONS

We have utilized combined experimental probes: x-ray diffraction, neutron diffraction and μSR to obtain the structural and magnetic properties in this iron-based spin ladder system, $BaFe_2Se_3$. The structural transition occurs at $P_s = 3.7(3)$ GPa from both neutron and x-ray diffraction measurements. The refined lattice constants as a function of applied pressures from XRD data are presented in Fig. 5 (c-d). The notion for lattice constants are used in the *Pnma* space group for consistency. The lattice constants at ambient pressure are $a(0) = 11.918(2)$Å, $b(0) = 5.446(2)$Å and $c(0) = 9.159(2)$Å. Across P_s, the principle change is a substantial reduction of lattice change along the out-of-ladder direction (a axis), which leads to a discontinuity in Fig. 5 (c). The corresponding lattice constant along a is comparable to the value in $BaFe_2S_3$[8]; while the values of 5.391(2)Å and 8.949(2)Å along the ladder and rung direction respectively are much larger than those in $BaFe_2S_3$ ($b = 5.288$Å and $c = 8.787$ Å). This might lead to the survival of the block type spin structure after the structural transition, which is stabilized mostly by the exchange interactions within the ladder plane[14,18]. In the isovalent substitution[35] of Se by S, the lattice along the rung direction shrinks faster than the out-of-ladder direction. Compared to that, under pressure the amount of suppression of the lattice constants in the ladder plane is much smaller than that along the out-of-ladder direction (Fig. 5 (d)), thus, the pressure is inadequate to induce the transformation to stripe order even up to our highest measured pressure. In the pressure region of 10-12 GPa, the lattice constants start to be close to the values in $BaFe_2S_3$, suggesting a potential magnetic phase transition or a coexistence of two magnetic phases around the superconducting phase predicted[10].

The μSR data reveal a smooth increase in T_N with increasing pressure up to the critical pressure of 3.7(3) GPa marking the structural transition. Such an effect could be associated with local lattice changes driven by pressure. To explore this, we fitted the Fe atomic coordinates (x, y, z) in the *Pnma* phase in the Rietveld refinements, in which the Wyckoff positions allow for a variation. These lead to the change of bond length between adjacent iron atoms along the ladder (u and v) and the rung (w). Their ratios $(\frac{u}{w}, \frac{v}{w})$ are plotted in Fig. 5 (e). The increase of $\frac{u}{w}$ and decrease of $\frac{v}{w}$ with increasing pressure indicate a clear tendency to form the block state. The same trend is observed at ambient pressure with decreasing temperature[12]. Such a strong change due to the magnetoelastic coupling may account for the enhancement of T_N.

Having established the influence of pressure on T_N, we now turn to the evolution of the ordered magnetic moment. We determined the magnetic order parameter from the NPD patterns as the integrated area of Q_{m1} (Fig. 3), normalized by the nearby nuclear Bragg peaks. The temperature dependence of the order parameter for

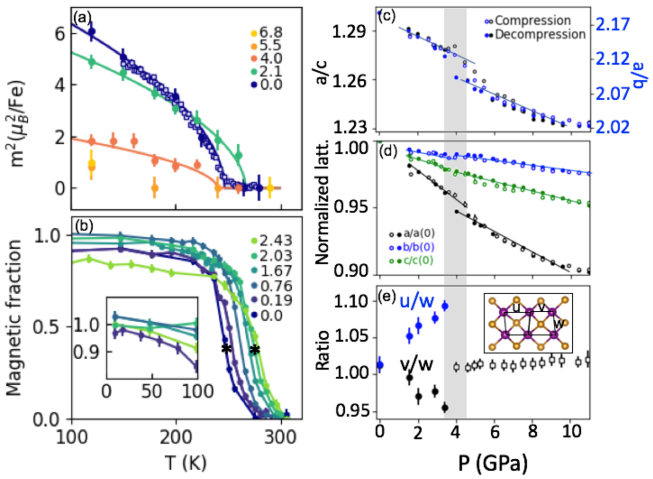

FIG. 5: (a) Square of the ordered magnetic moment (m^2) as a function of temperature for various applied pressures marked in the legend (units of GPa). The empty and filled symbols were obtained from neutron diffraction data collected on HB3A at HFIR and Pearl at ISIS, respectively. The solid lines are the results of power law fits of the form $m^2 \propto (T_c - T)^{2\beta}$. (b) Magnetically ordered volume fraction versus temperature determined from μSR measurements at the indicated pressures. The inset shows the magnetic fraction in the low temperature region. (c) Ratios between out-of ladder and within-ladder lattices (a/c and a/b). (d) Compressed (empty) and decompressed (filled) pressure-dependent lattice parameters normalized to the values at ambient pressure ($a(0) = 11.918(2)$Å, $b(0) = 5.446(2)$Å, $c(0) = 9.159(2)$Å). The solid lines are the results of linear fits. (e) Ratios of the Fe-Fe bond lengths along the ladder (u, v) and leg (w) direction as a function of decompressed pressure. Inset: the ladder plane in the *Pnma* phase. The shaded grey area marks the region of the structural transition P_s

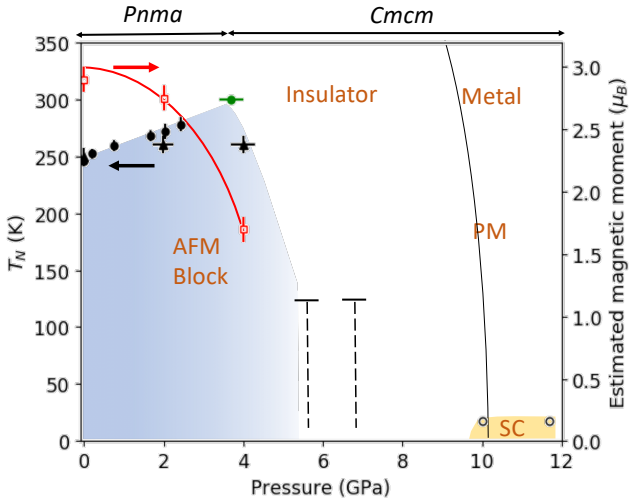

FIG. 6: Pressure versus temperature phase diagram for $BaFe_2Se_3$ constructed from experimental results in this and other work[10]. The antiferromagnetic (AFM) transition temperature T_N (black symbols, left axis) and estimated ordered moment (red symbols, right axis) are shown, with filled circles and triangles representing the μSR and neutron diffraction results, respectively. The horizontal lines at the pressures of 5.5 and 6.8 GPa mark the lowest measured temperature of 120 K, at which we observed block-type short range magnetic correlations. The bars indicate the upper limit for the onset of long range order. The green filled circle marks the structural transition ($P_s = 3.7(3)$ GPa) identified at room temperature, and AFM block-type magnetic order persists above P_s. The open circles denoting T_c and black line marking the metal-insulator transition are inferred from the literature[10].

all measured pressures is shown in Fig. 5 (a). Fitting to a simple power law provides an estimated critical exponent of 0.29(2), close to the value the 3D Ising value of 0.31. Comparison with the order parameter curve determined at ambient pressure, for which low-temperature data are available, allows us to estimate the low-temperature, saturated ordered moment at 2 and 4 GPa, as shown by the red squares in Fig. 6. The order parameter curves can be used to extract T_N as well; the results are plotted as black triangles in Fig. 6 and are consistent with the μSR results within the experimental uncertainty. For the last two pressures, 5.5 and 6.8 GPa, the symbols represent the upper boundary of the magnetic transition temperature, since we were not able to reach lower temperatures to determine the actual transition temperature.

By combining the experimental observations from XRD, NPD and μSR measurements under hydrostatic pressure on the same sample, we can establish the P-T phase diagram shown in Fig. 6. Despite their different structures at ambient pressure, $BaFe_2S_3$ and $BaFe_2Se_3$ exhibit superconductivity at similar pressures and T_c, as well as a common metal-insulator transition preceding the SC state. Another similarity is the initial enhancement of T_N[26,27] with increasing pressure, regardless of different types of AFM ordered states. This increase in T_N, which is not observed in dopant-suppressed magnetic order in other 2D iron-based superconductors (FeSCs), may imply strong magneto-elastic coupling inherent in the ladder system.

Several differences also exist between the two compounds. Along with its unusual block-type magnetism, $BaFe_2Se_3$ exhibits a potentially richer P-T phase diagram. The structural phase transition from the *Pnma* to the *Cmcm* phase at $P_s = 3.7(3)$ GPa is confirmed by both X-ray and neutron diffraction measurements. No such structural phase transition occurs in $BaFe_2S_3$, where the *Cmcm* structure is present from ambient pressure up to at least the highest measured pressure of 12 GPa[36]. In terms of the magnetic properties of $BaFe_2Se_3$, both the ordered moment m and T_N drop quickly above P_s. This might be associated with a Fe high-spin (HS) to low-spin (LS) transition induced by the structural transition which is also observed in FeS and FeSe[37,38]. Above P_s, the structure has a more compact stacking of ladders, as displayed in the variation of a/c or a/b versus P (Fig. 5(c)). The

abrupt shortening of the a axis is comparable with the case in FeS[39] where such shortening was accompanied by a pressure-induced HS to LS transition. Regardless of the large reduction of m and $T_{\rm N}$, the short-range block-type spin correlations remain present up to the highest measured pressure of 6.8 GPa. The robustness of the block magnetism in the $Cmcm$ phase, where the adjacent Fe-Fe distances are all equivalent, implies that its origin may strongly relate to the electronic and orbital degrees of freedom. The persistence of the block state is also consistent with the insulating properties predicted by theoretical calculations[40]. Despite the robust block state, the increase of $T_{\rm N}$ up to P_s followed by the more than 50% suppression of $T_{\rm N}$ within 1.5 GPa above P_s is incompatible with a scenario in which the essential block-type magnetic phase is stabilized simply by local magnetic exchange interactions, indicating perhaps another competing mechanism buried underneath the AFM block state.

V. CONCLUSIONS

Our results have vastly extended the range of pressures for which quantitative information exists on the structural phase transition and the evolution of the magnetic transition temperature and magnetic moment approaching the SC phase in the spin-ladder system $BaFe_2Se_3$. They have also made possible detailed comparisons with the sister compound $BaFe_2S_3$. The $BaFe_2Se_3$ P-T phase diagram displays persistent block magnetism across a wide pressure range, characterized by an initial increase in $T_{\rm N}$, followed by a strong reduction of $T_{\rm N}$ after the structural transition and a steadily reduced ordered moment with pressure. Such rich behavior is distinct from the case of the dopant dependent phase diagram in other FeSCs with a 2D square lattice[41], where the magnetic ordered phase is continuously suppressed close to the SC phase. This is associated with enhanced electron correlations in the quasi-1D ladder approaching the insulator-metal transition. The next frontier requires extending measurements into the SC phase starting from 10 GPa[10]. Whether the driving force of the superconductivity is induced by magnetic fluctuations due to the competition between block and stripe magnetic states proposed theoretically[40] or other electronic phases is still an open question.

VI. ACKNOWLEDGEMENT

The authors would like to acknowledge the beam line support from Martin Kunz and Andrew Doran at ALS, Gerald Morris at TRIUMF and Keith Taddei at HFIR. The authors would like to also thank STFC for provision of beam time at the ISIS Neutron and Muon Facility[42]. This work is funded by the U.S. Department of Energy, Office of Science, Office of Basic Energy Sciences, Materials Sciences and Engineering Division under Contract No. DE-AC02-05-CH11231 within the Quantum Materials Program (KC2202). M. W. and J. J. Y were supported by NSFC-11904414 and NSF of Guangdong under Contract No. 2018A030313055. S.K.L. was supported by an AAUW Dissertation Fellowship.

* Electronic address: shanwu@berkeley.edu

[1] D. B. McWhan, J. P. Remeika, T. M. Rice, W. F. Brinkman, J. P. Maita, and A. Menth, Phys. Rev. Lett. **27**, 941 (1971).

[2] D. B. McWhan, A. Menth, J. P. Remeika, W. F. Brinkman, and T. M. Rice, Phys. Rev. B **7**, 1920 (1973).

[3] Physics Reports **428**, 169 (2006), ISSN 0370-1573.

[4] B. Keimer, S. Kivelson, M. Norman, S. Uchida, and J. Zaanen, Nature **518**, 179 EP (2015).

[5] G. R. Stewart, Rev. Mod. Phys. **83**, 1589 (2011).

[6] P. Dai, Rev. Mod. Phys. **87**, 855 (2015).

[7] E. Dagotto, Rev. Mod. Phys. **85**, 849 (2013).

[8] H. Takahashi, A. Sugimoto, Y. Nambu, T. Yamauchi, Y. Hirata, T. Kawakami, M. Avdeev, K. Matsubayashi, F. Du, C. Kawashima, et al., Nature Materials **14**, 1008 (2015), ISSN 1476-1122.

[9] T. Yamauchi, Y. Hirata, Y. Ueda, and K. Ohgushi, Phys. Rev. Lett. **115**, 246402 (2015).

[10] J. Ying, H. Lei, C. Petrovic, Y. Xiao, and V. V. Struzhkin, Physical Review B Rapid Communication **95**, 241109(R) (2017).

[11] J. M. Caron, J. R. Neilson, D. C. Miller, A. Llobet, and T. M. McQueen, Phys. Rev. B **84**, 180409(R) (2011).

[12] Y. Nambu, K. Ohgushi, S. Suzuki, F. Du, M. Avdeev, Y. Uwatoko, K. Munakata, H. Fukazawa, S. Chi, Y. Ueda, et al., Phys. Rev. B **85**, 064413 (2012).

[13] T. Nagata, M. Uehara, J. Goto, J. Akimitsu, N. Motoyama, H. Eisaki, S. Uchida, H. Takahashi, T. Nakanishi, and N. Môri, Phys. Rev. Lett. **81**, 1090 (1998).

[14] M. Mourigal, S. Wu, M. B. Stone, J. R. Neilson, J. M. Caron, T. M. McQueen, and C. L. Broholm, Phys. Rev. Lett. **115**, 047401 (2015).

[15] S. Dong, J.-M. Liu, and E. Dagotto, Phys. Rev. Lett. **113**, 187204 (2014).

[16] N. D. Patel, A. Nocera, G. Alvarez, A. Moreo, S. Johnston, and E. Dagotto, Tech. Rep. (2018), 1807.10419v2.

[17] S. W. Lovesey, D. D. Khalyavin, and G. van der Laan, Physica Scripta **91**, 015803 (2016), ISSN 0031-8949.

[18] M. Wang, S. J. Jin, M. Yi, Y. Song, H. C. Jiang, W. L. Zhang, H. L. Sun, H. Q. Luo, A. D. Christianson, E. Bourret-Courchesne, et al., Phys. Rev. B **95**, 060502(R) (2017).

[19] E. J. König, A. M. Tsvelik, and P. Coleman, Phys. Rev. B **98**, 184517 (2018).

[20] T. Aoyama, S. Imaizumi, T. Togashi, Y. Sato,

K. Hashizume, Y. Nambu, Y. Hirata, M. Matsubara, and K. Ohgushi, Tech. Rep. (2019), 1902.10900v1.

[21] J. Herbrych, N. Kaushal, A. Nocera, G. Alvarez, A. Moreo, and E. Dagotto, Nature Communications p. 3736 (2018), ISSN 2041-1723.

[22] K. Takubo, Y. Yokoyama, H. Wadati, S. Iwasaki, T. Mizokawa, T. Boyko, R. Sutarto, F. He, K. Hashizume, S. Imaizumi, et al., Phys. Rev. B **96**, 115157 (2017).

[23] Q. Luo, A. Nicholson, J. Rincón, S. Liang, J. Riera, G. Alvarez, L. Wang, W. Ku, G. D. Samolyuk, A. Moreo, et al., Phys. Rev. B **87**, 024404 (2013).

[24] J. Rincón, A. Moreo, G. Alvarez, and E. Dagotto, Phys. Rev. Lett. **112**, 106405 (2014).

[25] S. Chi, Y. Uwatoko, H. Cao, Y. Hirata, K. Hashizume, T. Aoyama, and K. Ohgushi, Phys. Rev. Lett. **117**, 047003 (2016).

[26] L. Zheng, B. A. Frandsen, C. Wu, M. Yi, S. Wu, Q. Huang, E. Bourret-Courchesne, G. Simutis, R. Khasanov, D. X. Yao, et al., Physical Review B **98**, 18 (2018), ISSN 24699969, 1807.10703.

[27] P. Materne, W. Bi, J. Zhao, M. Y. Hu, M. L. Amigó, S. Seiro, S. Aswartham, B. Büchner, and E. E. Alp, Physical Review B **99**, 020505(R) (2019), ISSN 2469-9950.

[28] B. Saparov, S. Calder, B. Sipos, H. Cao, S. Chi, D. J. Singh, A. D. Christianson, M. D. Lumsden, and A. S. Sefat, Phys. Rev. B **84**, 245132 (2011).

[29] C. L. Bull, N. P. Funnell, M. G. Tucker, S. Hull, D. J. Francis, and W. G. Marshall, High Pressure Research **36**, 493 (2016).

[30] R. Khasanov, Z. Guguchia, A. Maisuradze, D. Andreica, M. Elender, A. Raselli, Z. Shermadini, T. Goko, F. Knecht, E. Morenzoni, et al., High Pressure Research **36**, 140 (2016).

[31] J. Rodriguez-Carvajal, in *Satellite meeting on powder diffraction of the XV congress of the IUCr* (Toulouse, France:[sn], 1990), vol. 127.

[32] V. Svitlyk, G. Garbarino, A. D. Rosa, E. Pomjakushina, A. Krzton-Maziopa, K. Conder, M. Nunez-Regueiro, and M. Mezouar, Journal of Physics: Condensed Matter **31**, 085401 (2019).

[33] J. M. Caron, J. R. Neilson, D. C. Miller, K. Arpino, A. Llobet, and T. M. McQueen, Phys. Rev. B **85**, 180405(R) (2012).

[34] A. Suter and B. Wojek, Physics Procedia **30**, 69 (2012).

[35] J. Yu, J. Yin, H. Sun, B. A. Frandsen, S. Wu, M. Yi, Q. Huang, E. B. Courchesne, R. J. Birgeneau, and M. Wang, In preparation (2019).

[36] K. Kobayashi, S. Maki, Y. Murakami, Y. Hirata, K. Ohgushi, and J. ichi Yamaura, Superconductor Science and Technology **31**, 105002 (2018).

[37] J.-P. Rueff, C.-C. Kao, V. V. Struzhkin, J. Badro, J. Shu, R. J. Hemley, and H. K. Mao, Phys. Rev. Lett. **82**, 3284 (1999).

[38] B. W. Lebert, V. Balédent, P. Toulemonde, J. M. Ablett, and J.-P. Rueff, Phys. Rev. B **97**, 180503(R) (2018).

[39] Y. Fei, C. T. Prewitt, H.-k. Mao, and C. M. Bertka, Science **268**, 1892 (1995), ISSN 0036-8075.

[40] Y. Zhang, L.-F. Lin, J.-J. Zhang, E. Dagotto, and S. Dong, Phys. Rev. B **97**, 045119 (2018).

[41] R. M. Fernandes, A. V. Chubukov, and J. Schmalian, Nature Physics **10**, 97 (2014), ISSN 1745-2473.

[42] S. Wu, C. L. Bull, T. R. Forrest, J. Yin, B. Frandsen, and R. J. Birgeneau, STFC ISIS Neutron and Muon Source (2018), URL `https://doi.org/10.5286/ISIS.E.RB1810189`.